The RHESSI Imaging Concept

G. J. Hurford[1],E. J. Schmahl[2], A. J. Conway[3], B. R. Dennis[4], R. A. Schwartz[4,5], R. P. Lin[1], J. McTiernan[1], D. M. Smith[1], C. Johns-Krull[6], A. Csillaghy[7], M. J. Aschwanden[8], T. R. Metcalf[8]
[1]*Space Sciences Laboratory, University of California Berkeley, Berkeley, CA*
[2]*Astronomy Department, University of Maryland, College Park, MD 20742*
[3]*Department of Physics and Astronomy, The Open University, Milton Keynes MK7 6AA, UK*
[4]*Lab for Astronomy and Solar Physics, NASA Goddard Space Flight Center, Greenbelt, MD 20771*
[5]*SAIC,*
[6]*Department of Physics and Astronomy, Rice University, Houston, TX, 77005*
[7]*University of Applied Sciences, CH-5210 Windisch, Switzerland*
[8]*Lockheed Martin Advanced Technology Center, Solar & Astrophysics Laboratory, Dept. L9-41, Palo Alto, CA 94304*

2002/08/08

Abstract.
The Reuven Ramaty High Energy Solar Spectroscopic Imager (*RHESSI*) images solar hard X-rays and gamma-rays from 3 keV to 15 MeV with spatial resolution as high as 2.3 arcseconds. Instead of using conventional optics, imaging is based on nine rotating modulation collimators that time-modulate the incident flux as the spacecraft rotates. Starting from the arrival time of individual photons, ground-based software then uses the time-modulated signals to reconstruct the image of the source.

The purpose of this paper is to convey both an intuitive feel and the mathematical basis for this imaging process. Following a review of the relevant hardware, the imaging principles and the basic back-projection method are described, along with their relation to Fourier transforms. Several specific algorithms (CLEAN, MEM, PIXONS and Forward-Fitting) applicable to *RHESSI* imaging are briefly described. The characteristic strengths and weaknesses of this type of imaging are then summarized.

Keywords: Sun : X-rays — Sun : Flares — Instruments — Image Processing — Numerical Methods

1. Introduction

The primary scientific objective of the Reuven Ramaty High Energy Solar Spectroscopic Imager (RHESSI) is the study of energy release and particle acceleration in solar flares. This is accomplished by imaging-spectroscopy of solar hard X-rays and gamma-rays over a 3-keV to 15-MeV energy range with energy resolution of $\sim$1 keV, time resolution of $\sim$2 s or better and spatial resolution of 2.3 arcseconds.

The only practical method of combining such angular resolution with high sensitivity in this energy regime and within the cost, mass and launch constraints of a small satellite is to use collimator-based Fourier-transform imaging. (See Prince *et al.*, 1988 for a review of imaging techniques.) One of the most powerful of the Fourier family of techniques is rotational modulation synthesis, first proposed by Mertz (1967) and implemented by Schnopper *et al.* (1968) for non-solar observations.

In a solar context, previous related instrumentation included the Hard X-ray Imaging Spectrometer (HXIS) (Van Beek *et al.*, 1980), a direct-imaging hard X-ray telescope flown on the Solar Maximum Mission. Although its multigrid collimator achieved 8 arcsecond resolution, its one-to-one association of imaging pixels to detector elements seriously limited its sensitivity. A Rotating Modulation Collimator (RMC) was used for solar flare X-ray imaging on the Hinotori mission telescope (Makashima *et al.*, 1977; Ohki *et al.*, 1982; Enome, 1982), with angular resolution of $28''$ in the 20-40 keV energy range. Subsequently, the Hard X-ray Telescope (HXT) on the Yohkoh satellite used non-rotating Fourier synthesis with angular resolution of $\sim 8''$ in the 20-100 keV energy range (Kosugi *et al.*, 1991). A balloon-borne solar rotation modulation telescope, the High Energy Imaging Device (HEIDI) (Crannell *et al.*, 1994) was used as a vehicle for making several important engineering advances in this area, including the demonstration of a high-bandwidth, high-resolution solar aspect system and the development of error-analysis techniques for the RMC optical design.

Among the new features of *RHESSI* imaging are its high ($2.3''$) angular resolution, its use of aspect knowledge in place of precision pointing, its wide energy range viewed with a common set of 'optics', its relative immunity to alignment errors and its ability to self-calibrate its instrumental response.

An overview of the *RHESSI* mission is provided by Lin *et al.*, 2002. The purpose of this paper is to describe the concepts and techniques of RMC imaging as implemented on *RHESSI* with the hope that an intuitive understanding of the strengths and weaknesses of these techniques may prove useful both to the making and evaluating the results of such imaging for the analysis of solar flares.

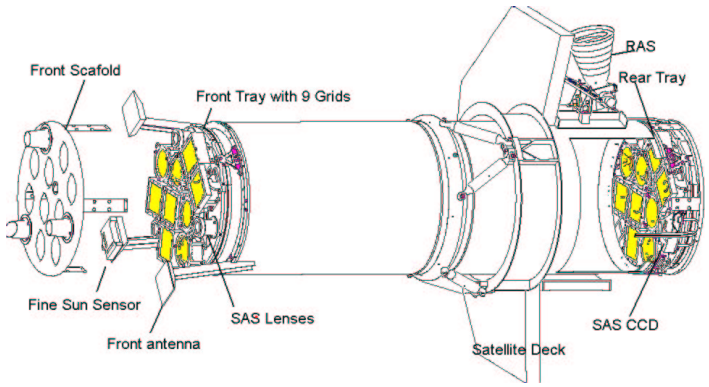

Figure 1. Perspective of the *RHESSI* Telescope. The key imager components are two identical sets of nine grids, mounted on the front and rear grid trays. A corresponding set of nine germanium detectors (not shown) is mounted behind the rear grids. The solar aspect system (SAS) consists of three lenses mounted on the front grid tray which focus optical images onto SAS CCD's on the rear grid tray.

2. The *RHESSI* Imager–A Brief Hardware Description

2.1. The Subcollimators

The *RHESSI* imaging hardware is described in detail by Zehnder, Fivian and Henneck, 2002. A schematic view, shown in Figure 1, shows a set of nine bi-grid collimators, each consisting of a pair of widely separated grids in front of a non-imaging X-ray/gamma-ray detector. Each grid consists of a planar array of equally-spaced, X-ray-opaque slats separated by transparent slits. The slits of each pair of grids are parallel to each other and their pitches (p) are identical.

As illustrated in Figure 2, the transmission through the grid pair depends on the direction of the incident X-rays. If the direction of incidence is changed as a function of time, the transmission of the grid pair is modulated in time as the shadow of the slits in the top grid alternately overlays the slits or slats in the rear grid. For slits and slats of equal width, the transmission is time-modulated from zero to 50% and back to zero. One cycle of this periodic transmission occurs for a change in source angle (in the plane orthogonal to the slits) of p/L where L is the separation between grids (1550 mm). The angular resolution is defined as $p/(2L)$. For off-axis sources, changing the angle between the source and collimator is achieved by rotating the spacecraft at about 15 revolutions per minute. The nominal parameters of the *RHESSI* grids are listed in Table 1. Details of the grid geometry, calibration and

response as a function of energy are given in a forthcoming paper by Hurford *et al.*

Table I. RHESSI – Nominal Grid Parameters

Subcollimator Number	1	2	3	4	5	6	7	8	9
Pitch (mm)	0.034	0.059	0.102	0.177	0.306	0.530	0.918	1.590	2.754
Slit Width (mm)	0.020	0.035	0.061	0.106	0.184	0.318	0.477	0.811	1.487
FWHM Resolution (arcsec)	2.26	3.92	6.79	11.76	20.36	35.27	61.08	105.8	183.2
Max. Transmission	0.60	0.60	0.60	0.60	0.60	0.60	0.52	0.51	0.54
Grid thickness (mm)	1.2	2.1	3.6	6.2	10.7	18.6	6.2	6.2	30.0
Slat Material	Mo	W	W	W	W	W	W	W	W
Field of View (degrees)	1.0	1.0	1.0	1.0	1.0	1.0	4.4	7.5	2.8

2.2. Other Subsystems

The role of the detector and data system is to record the arrival time and energy of each photon detected, allowing the modulated count rate to be determined as a function of rotation angle.

The detectors, described by Smith *et al.* (2002), are high-purity germanium crystals, each electrically divided into front and rear segments. The front segment is sensitive from ∼3 keV to ∼200 keV while the thicker rear segment continues the response to 15 MeV while being shielded from the potentially intense flux of low-energy X-rays. Since the detectors have no spatial resolution, they were optimized for high sensitivity and energy resolution. The detectors are mounted in a cryostat in which they are mechanically cooled to ∼75 K.

The detector output pulse for each detected photon is amplified, shaped and digitized, and passed to the Instrument Data Processing Unit (IDPU) (Curtis *et al.*, 2002). The IDPU stores each datum as a 32-bit event word incorporating the detector ID, a 14-bit energy tag and the arrival time. This time is noted with 1 microsecond resolution to enable all combinations of coincidence events to be inferred during data analysis. A 4-Gbyte solid-state recorder, corresponding to almost $\sim 10^9$ events, stores the data for periodic downloading. As described by Bester *et al.* (2002), an average of about 1.8 Gbytes per day is transmitted.

A high-bandwidth solar aspect system (SAS) (Zehnder *et al.*, 2002) permits substitution of accurate pointing knowledge for pointing stability, which need only be controlled to arcminutes. The SAS consists

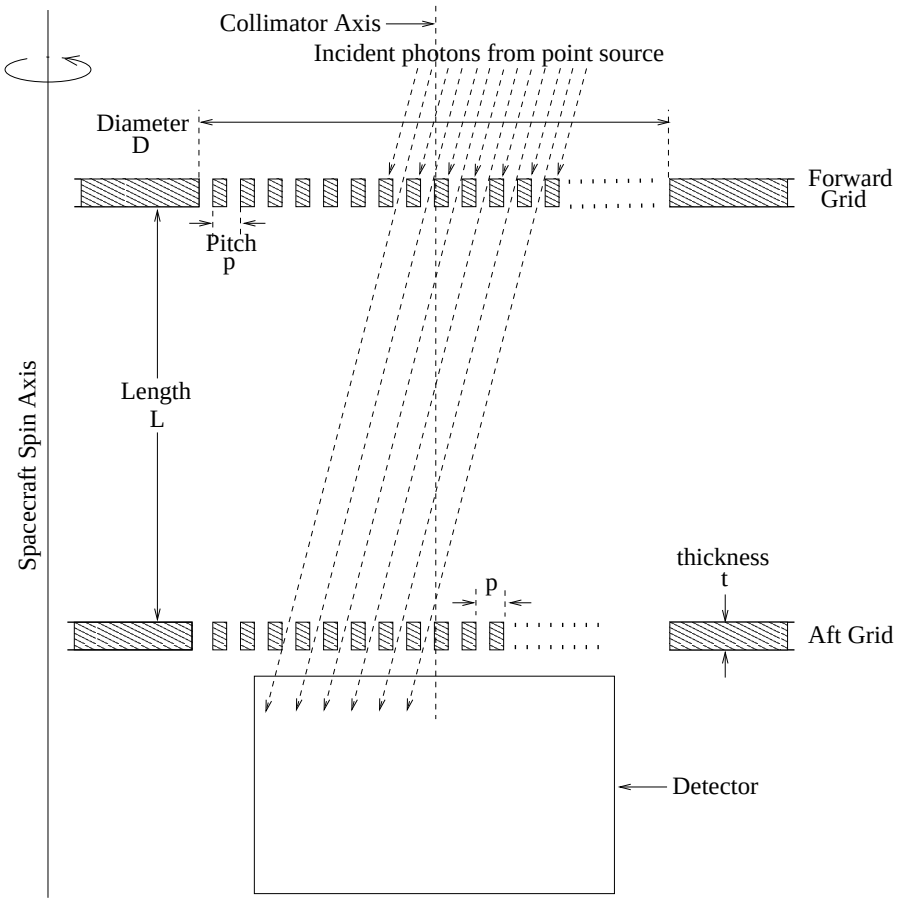

Figure 2. Schematic geometry of the *RHESSI* subcollimators, showing representative incidence of photons with respect to the collimator axis.

of 3 lenses in the front grid plane that focus solar images onto a set of 3 linear diode arrays in the rear grid plane. The solar limb is determined at 6 positions at rates up to 128 Hz, giving pitch and yaw to $\sim 0.4'' rms$. Roll aspect is provided by one of two roll aspect sensors. Imaging to date has used a photo-multiplier tube based system (PMTRAS), described by Hurford and Curtis (2002). This system notes the times at which bright stars are detected in the plane perpendicular to the earth-Sun line to determine absolute roll to $\sim$ 1 arcminute. An alternate roll aspect system (RAS) (Zehnder *et al.*, 2002), based on a similar concept but using a linear photodiode, is also available.

The data handling concept outlined above must accomodate high count rates where the finite reponse time of the detector and data handling system become relevant (Smith *et al.*, 2002). This accomo-

dation employs four techniques, the goals of which are to preserve the sensitivity to rare high-energy gamma rays while maintaining the ability to image lower energy X-rays, whose incident count rate can be ∼12 orders of magnitude higher.

The first technique is to apply corrections for the estimated dead time of the detector/electronics. Spare bits in the event words are used to encode the dead time with 512 microsecond time resolution, so as to follow the effects of modulation.

Second, as the dead time becomes larger, on-board software commands either or both of two sets of nine aluminum attenuators to be mechanically inserted between the rear grids and the detectors. The attenuators preferentially reduce the flux of low-energy photons while having no effect over ∼100 keV.

Third, when count rates become sufficiently high that they do not adequately characterize the modulation, an additional data handling method, capable of handling higher count rates, is automatically activated. In this 'fast rate mode', undigitized front detector counts are binned into 4 energy channels with time bins that are sufficiently short so as to preserve the modulation. This permits imaging at higher count rates than photon tagging.

The fourth and final feature is used to deal with the finite memory size. As the memory becomes filled, a decimation scheme is enabled which digitally discards a fixed fraction of front-segment events below an energy threshold. Both the fraction and the energy thresholds are programmable. Although the discarding does not bias the characterization of the modulation, it does compromise the use of front-rear concidences.

Two features of the detector response, discussed by Smith *et al.* (2002), are particularly relevant in practice in an imaging context. The first is that substantial data gaps (up to several hundred milliseconds) are observed. Since these gaps have a characteristic signature, the time and duration of their occurrence can be 'predicted' and are interpreted as periods of zero live time. The second is pileup (whereby two or more low-energy photons arrive simultaneously and are indistiguishable from a single high-energy photon), which has long been a complication for spectroscopy. Pileup also introduces artifacts in the imaging as well at very high count rates. Since pileup counts are generated at a rate corresponding to the square of the detected low-energy count rates, the pileup counts are also modulated. This can result in 'ghost images' representing low-energy photons appearing in images nominally formed from high-energy photons.

3. Modulation Principles

3.1. The Modulation Profile

As we have seen the *RHESSI* imaging hardware uses a set of rotating collimators to time-modulate the detected flux. To understand how this encodes imaging information, it is conceptually useful to adopt the perspective of a rotating coordinate system fixed on the collimator (as in Figure 2). In the typical case of a source that is slightly offset from the collimator axis, the source then moves in a circle about this axis. The component of source motion parallel to the slits does not cause modulation so that the only relevant component of the source motion is its simple harmonic motion perpendicular to the slits. For a single source, the various panels in Figure 3 show how the resulting modulated count rates (modulation profiles) depend on the source intensity, location and size. In practice, however, there are multiple sources, whose sum yields an observable waveform as shown in the last panel in Figure 3. Thus the central data analysis task for *RHESSI* imaging is the inverse problem of deducing the source geometry, given a set of observed modulation profiles from the different subcollimators. Much of the remainder of this paper will be devoted to the approaches taken to the solution of this problem.

We can set the stage for solving this inverse problem by digitizing the modulation profile into a series of time bins, and by describing the brightness distribution in the source plane as a pixelized image F_m, where F_m is the photon flux (photons cm^{-2} s^{-1}) from pixel m incident on the *RHESSI's* front grids.

Then the following formal equation shows that the expected counts in the ith time bin is given by:

$$\mathcal{C}_i = A \sum_m P_{im} F_m \Delta t_i \tag{1}$$

In this notation, P_{im} is the probability that a photon originating in a pixel m and incident on the front grid will be counted in the ith time bin during interval Δt. (Note that since m is the index of a two-dimensional map, P_{im} is really a numerical "cube".) Since P_{im} can be calculated from a knowledge of the grid properties and collimator aspect, the inverse problem can be summarized as: Given a measurement of count rates $\mathcal{C}_i$ in each time bin, find the source map, F_m.

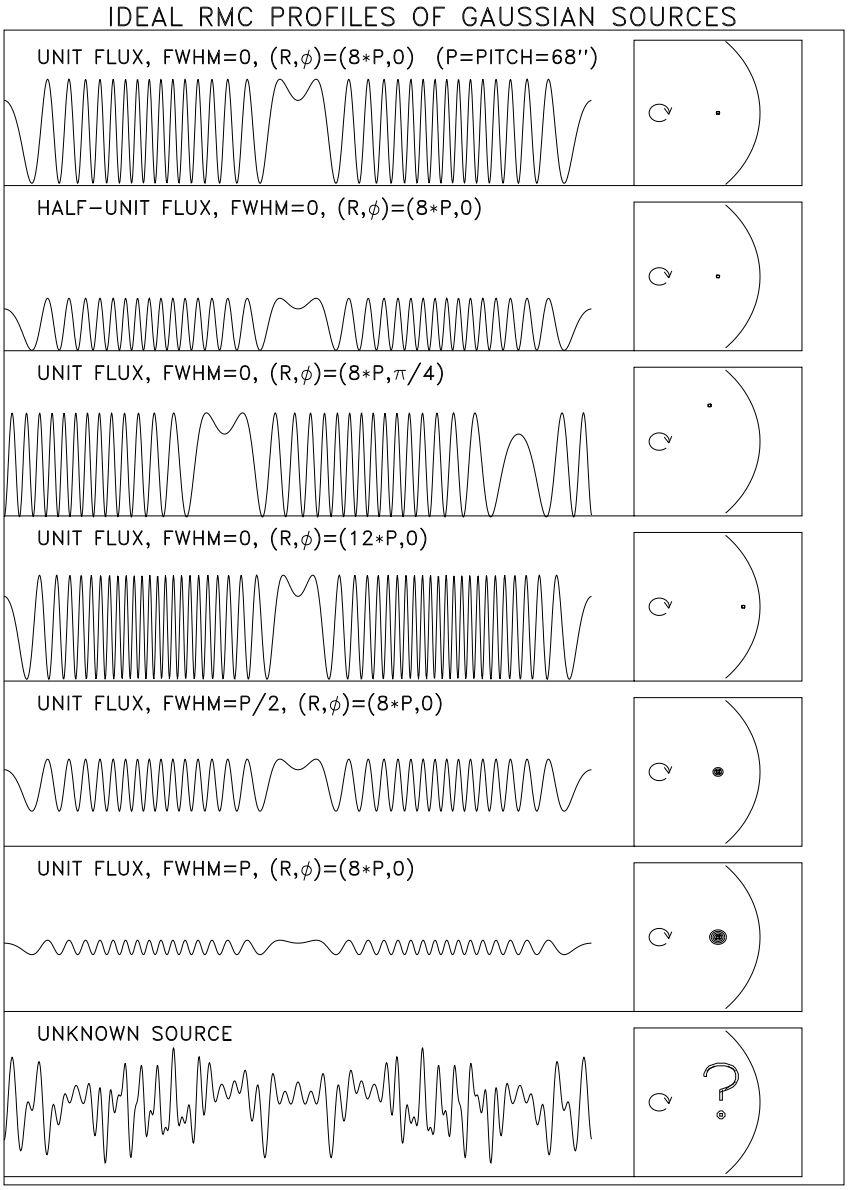

Figure 3. Modulation profiles for various configurations of an off-axis source as transmitted through ideal grids with equal slits and slats mounted on a collimator that is rotating uniformly about a fixed axis. Successive panels show the effect of changing source characteristics on the modulation profile. The first panel shows the modulation profile of a single point source. The second panel assumes a source with the same location, but one half of the intensity. Since the response of the the collimator/detector system is linear, changing the intensity of the source just decreases the amplitude of the modulation without changing its shape. The third panel shows that the effect of shifting the source azimuthally shifts the modulation pattern in time. Moving the original source further off-axis increases the number of modulation cycles per rotation as shown in panel 4. Increasing the diameter of the source (while keeping its total intensity the same) reduces the amplitude of the modulation while retaining the same time-averaged transmission (panel 5). For sources that are large compared to the resolution of the collimator, reduces the modulation still further (panel 6). The final panel shows a typical modulation pattern from a more complex source, which might represent the superposition of several point sources.

3.2. Describing the Grid Response

The solution of the inverse problem posed by Equation (1) requires a knowledge of P_{im}, the probability that a photon from map pixel, m, will be detected in the i'th time bin. This requires calculation of the transmission probability of a grid pair as a function of energy and the precise direction of incidence. In this section, we describe the approach taken to accomplish this in the case of *RHESSI*.

To introduce this issue, we return briefly to the idealized case of thin, opaque grids with equal slits and slats, for which the modulation takes on a characterisitic 'triangle-like' form as suggested by Figure 3. Since this time profile is periodic, the transmission probability can be described in terms of the first few harmonics of its expansion as a Fourier cosine series containing only odd harmonics:

$$P_{triangle}(\Phi) = \frac{1}{4}\cdot(1+\frac{8}{\pi^2}cos(\Phi)+\frac{8}{9\pi^2}cos(3\Phi)+\frac{8}{25\pi^2}cos(5\Phi)+\cdots) \quad (2)$$

where $\Phi = 2\pi\theta L/p$. (p is the grid pitch; L is the distance between front and rear; θ is the angle of incidence in the x-z plane which can be readily calculated from the location of each pixel.) This is equivalent to the form used by Schnopper *et al.* (1970) for their observations of galactic-center with a rocket-borne RMC.

There are several reasons why the triangular functions described by Equation (2) cannot be applied to *RHESSI*: as photon energies increase, the grids become transparent; the slits and slats are, in general, not equal; the peak transmissions are decreased by internal shadowing within the each grid due to the large ratio of slit width to grid thickness; the grids have imperfections, due both to fabrication tolerances and to structural design features. Furthermore, these effects are not independent since, for example, some moderate energy photons, incapable of penetrating the grids directly, could penetrate the corner of a slat when they are incident from a few arcminutes off-axis.

In previous missions such as Yohkoh HXT represents, these effects were not as severe so were accomodated by modifying the triangular functional form and introducing more parameters (Sato, Kosugi and Makishima, 1999). However, for *RHESSI* a different approach is necessary. All the factors identified above can be quantitatively described by generalizing the idealized Fourier expansion of the grid transmission into the form,

$$P(\Phi) = T\cdot(1+a_1\ cos[\Phi-\Psi_1]+a_2\ cos(2[\Phi-\Psi_2])+a_3\ cos(3[\Phi-\Psi_3])+\cdots) \quad (3)$$

where T is the average collimator transmission, a_i and psi_i are relative modulation amplitudes and phases. For ideal grids, these parameters would have fixed values, but for *RHESSI*, T and the other coefficients become slowly varying functions of map position and energy. Note that the expansion includes terms with even as well as odd harmonics. (The grid response is discussed in detail by Hurford *et al.*) Use of the higher-order terms is in fact desirable since in principle, the next harmonics effectively increase the angular resolution of each grid by factors of 2 and 3! For most imaging applications, and in the remainder of this paper we will assume that only the fundamental term is used. Because of the 'orthogonality' of the harmonics, this simplification introduces no 'bias', and only slightly degrades the signal-to-noise. In summary then, the characteristics of real grids can be accomodated by treating the idealized triangles as sinusoids, whose amplitude for each grid depends on energy and direction of incidence. Also, as we shall see, this approximation also enables considerable computational efficiency in the imaging algorithms.

3.3. The Modulation Pattern

In the preceding section, we have described the *modulation profile* as the one-dimensional function of count rate vs time induced by the relative motion of source with respect to the grids. In this section, we introduce an additional concept, the *modulation pattern*, which is a two-dimensional map characterizing the instantaneous response of a subcollimator. Roughly speaking, it can be thought of as a probability map on the Sun of the possible origin of a photon that was detected at a specific time. The *modulation pattern* is a useful concept found, in in one guise or another, in other domains of Fourier imaging. In the case of Yohkoh/HXT, there are 64 fixed *modulation patterns*, each corresponding to one of 64 collimator pairs. In radio astronomy, the *modulation pattern* is a projection of the complex *fringe pattern*, which will be referred to in the Appendix on visibilities. Since *RHESSI's* nine subcollimators are rotating and have a response which varies slowly with energy and time, there can be a very large number (thousands) of modulation patterns. It is easy to see that each *modulation pattern* takes the form of equally-spaced "stripes", whose contours have constant phase Φ, and that the cross-section perpendicular to each "stripe" is the (nearly) triangular waveform given by Equation (2).

In principle, image reconstruction based on inverting Equation (1) would require repeated calculation or temporary storage of the two-dimensional modulation profile, P_{im}, for each time bin and each pixel.

In practice, the computation and storage requirements render this impractical. Two simplifications are used to deal with this. First, the mapping is done in polar coordinates, with an arbitrary origin, well outside the mapping field of view. Second, the instrument response is calculated in terms of 'universal modulation patterns'. One such pattern represents the set modulation pattern (in polar coordinates) in a rotating coordinate system. The second pattern is the same, except for a 90-degree phase shift. The result is that the modulation pattern at any instant can be represented by the weighted sum of a subset of the elements of the precalculated 'universal modulation pattern'. Although this approach saves an order of magnitude in computation time and memory, the remainder of the discussion of modulation patterns will neglect this, since in practice, it is tranparent to the user.

There is an intimate relationship between the P_{im} "cube" for profiles mentioned above and the *modulation pattern*. If one chooses a value of i (*i.e.*, a single time bin), then the modulation pattern is proportional to the two-dimensional map P_{im}, where each pixel is indexed by m (x_m, y_m). By Equation (1e), at each time bin, the count rate is a weighted scalar product of the *modulation pattern* and the true source map F_m.

This can be expressed mathematically in terms of the roll angle, the amplitude coefficients a_n, and phases Ψ_n. Taking the telescope as our reference frame, we let a point source move on a circle (roll angle $\alpha = 0 - 2\pi$) in the source plane. For an ideal RMC (idealized grids, steady spin), the argument Φ in Equation (2) is

$$\Phi = Kx = Kr\cos\alpha \tag{4}$$

where the source is at radial position r in the sky plane, and the wavenumber of the detector is $K = 2\pi/p$.

Note that $\cos\alpha$ is present because the modulation described by Equation (2) only depends on the phase Φ of the source. The effect of this factor can be regarded as changing the "effective pitch" $p\sec(\alpha)$.

For a given map center, the quantities (a_n, T, and Ψ_n) are computed from the aspect system and the grid response matrices. The function P_{im} is computable for any time interval (i) and any point source (m) on the Sun. Therefore, since the signal expected for a superposition of sources is the superposition of point source signals, any model source can be used to predict a modulation profile. This is the basis for all *RHESSI* reconstruction algorithms and underlies Equation (3).

In general, if detector k is at roll angle α_i, and the point source has position vector (x_0, y_0) in the source plane, with polar equivalent (r_0, ϕ_0), then the generalization of the phase Φ in Equation (4) is:

$$\Phi_{ik} = \mathbf{K}_{ik}.\mathbf{r} = (K_k \cos\alpha_i)x_0 + (K_k \sin\alpha_i)y_0 = K_k r_0 \cos(\alpha_i - \phi_0) \quad (5)$$

The set of photon arrival times taken from the *RHESSI* telemetry can be histogrammed to yield a raw count rate profile. The *RHESSI* user can select an almost arbitrary set of time bin sizes $\{\Delta t_i\}$ for histogramming. (Δt_i is necessarily $\geq 1\ \mu s$, and may be as large as $\sim 1\ s$, but is more typically $\sim 0.5\ ms$.) After the time bin selection, the count/bin profile becomes a function of roll angle α, and one can proceed to calibrate the count rates. The size of the time bins depends on the detector, with the finest detectors (smallest p) requiring the smallest time bins.

3.4. The Response Geometry

For phase and amplitude calibration, that is determining (a_n, Ψ_n), one must first select a center for the mapping. Figure 4 shows the contours of the subcollimator phases and map center at one instant of rotation. The lines of constant phase for a subcollimator of angular pitch p are separated by $2\pi R/p$ radians, the map being centered at a distance R from the spin axis. The phase at map center rises and falls in a quasi-sinusoidal way (precisely sinusoidal if there is no drift or wobble in the pointing) during the spacecraft rotation.

Although the selected map center is arbitrary, it should be close to the centroid of source of emission. This is because the map center is used as the basis for determining the grid response parameters, which are then assumed to be uniform over the mapped field of view. In practice, the map center can be found in several ways (coarse mapping, context observations or using previous knowledge of the flare position).

4. Image Reconstruction

In this section we review the various image reconstruction algorithms that are used for *RHESSI* imaging. The general approach is that one uses a 'back projection' algorithm to generate an initial estimate of the image. This estimate represents a convolution of the source with the instrumental response and so may have significant sidelobes. To improve the image quality (viz. to reduce the sidelobes), one can then use a variety of techniques. Each of these other techniques(CLEAN, MEM, MEMVIS, PIXONS, Forward-Fitting) make broad assumptions about the character of the source, and most proceed in a cycle of

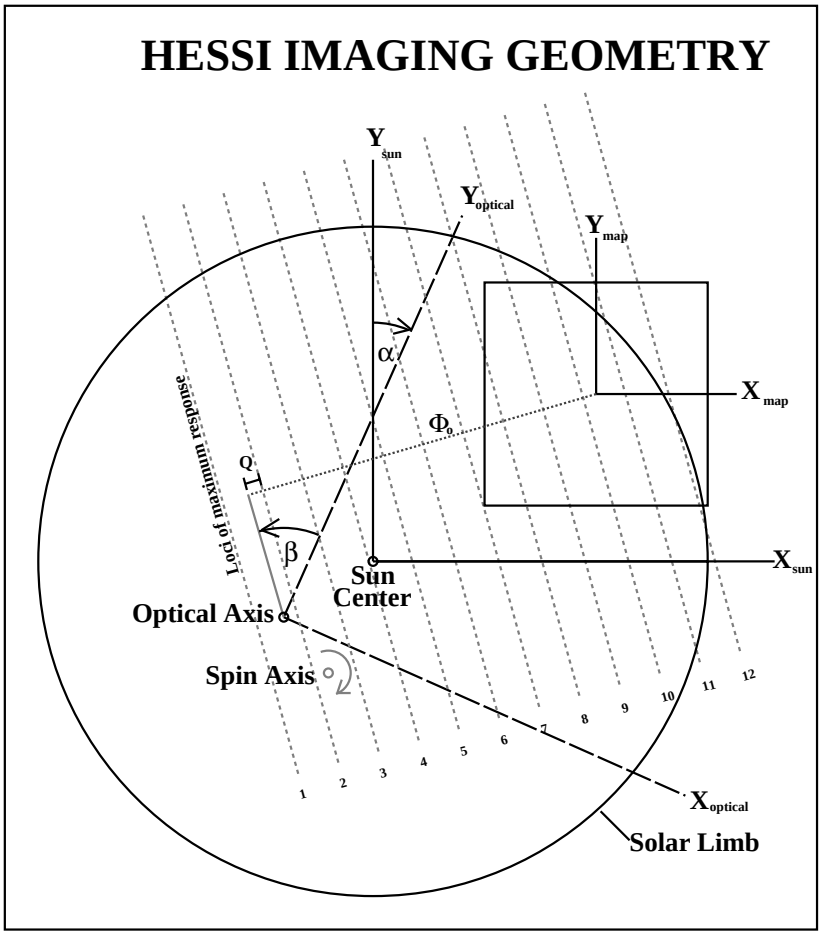

Figure 4. Lines of constant phase for one subcollimator at one instant of rotation projected on the solar disk. The spacecraft coordinate system rotates clockwise (increasing α), and the lines of constant phase lie at a constant angle β relative to the spacecraft coordinates. The phase contours, shown by the parallel dashed lines numbered 1,2,3,$\cdots$, represent contours of constant phase and are separated by multiples 2π radians in phase from the subcollimator line of maximum response.

predicting the modulation profile for the test image, comparing the predicted and observed modulation profiles, modifying the test image, and iterating.

4.1. Back Projection and Fourier Transforms

Back projection (Mertz, Nakano and Kilner, 1986) is the most straightforward and basic method of image reconstruction. It is equivalent to a 2D Fourier transform (Kilner and Nakano, 1989). A map constructed by this method is called the "dirty map", being the analogue of the radio astronomer's initial Fourier transform of the observed visibilities. Back projection is a linear process: maps for arbitrary time intervals may be added together, and maps for different pitches and harmonics may be summed, generally leading to improvement of the image. Further improvements to the image by CLEAN or MEM (for example) do not share this property of linearity.

As we have seen, for a given instant in time, the response of a detector to a source flux distribution is its modulation pattern rotated to the roll angle for that time. Detected photons are most likely to have come from regions where the modulation pattern has its highest values. Back projection creates an image by distributing the received photons onto a map according to the modulation pattern. In fact, based on one time bin alone back projection gives an image that is identical to the modulation pattern. For many time bins, back projection simply involves averaging the modulation patterns, weighting each one according to the the number of photons received in that time bin. Of course, in spreading flux across an image in this way some of it will be misplaced. This is most obvious for the case of a point source, where photons have come from only one point, but will be traced back to many different regions by back projection. Despite this, given many time bins and several detectors, the greatest concentration of flux will usually be at the location of the point source. In essence, back projection is analogous to performing an inverse Fourier transform, and the problems caused are a result of having insufficient coverage in Fourier space.

Mathematically, back projection can be described as follows. The modulation patterns P_{im} are computed for all roll angle α_i and map pixels m. Then they are normalized according to a recipe described by Durouchoux *et al.* (1983): (a) Subtract out the mean over roll angles at each pixel: ($\widetilde{P}_{im} = P_{im} - < P_m >$). (b) Then divide each value by its variance over roll angles: ($\widehat{P}_{im} = \widetilde{P}_{im} / < \widetilde{P}_m^2 >$).

(In practice, a slightly more complex formulation is used, in order to distinguish the variance component due to modulation from the variance component due to the slower changes in transmission of individual grids caused by internal shadowing.) The brightness D_m of each pixel (m) in the back-projection map is defined by the following linear combination of the count rates $\mathcal{C}_i$:

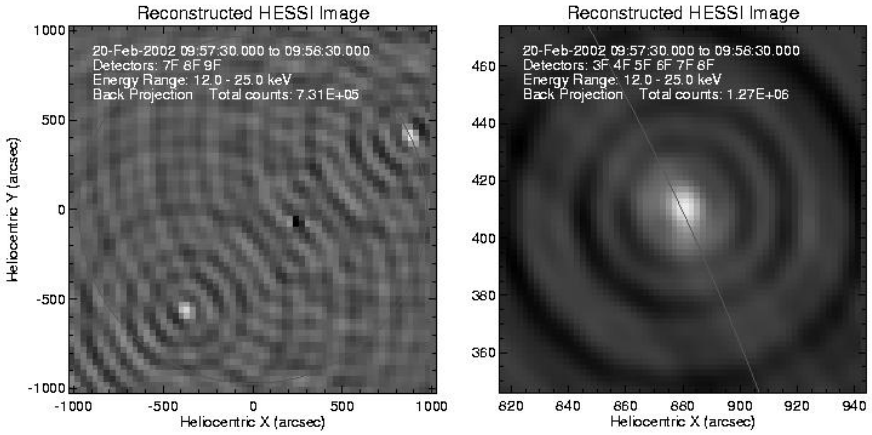

Figure 5. Full-Sun and small-field back-projection images for a *RHESSI* flare.

$$D_m = \frac{1}{A}\sum_{i=1}^{N}[\mathcal{C}_i/\Delta t]\cdot\widehat{P}_{im} \tag{6}$$

where A is the effective area (cm^2) of the detector and Δt is the time bin duration (s). The initial Durouchoux normalization and the division by $A\Delta t$ ensures that the peak of the dirty map equals the strength of a dominant source. The map then has units of counts cm^{-2} s^{-1}.

Figure 5 shows an example of a back-projection image for a compact flare source whose size is smaller than the subcollimator's angular resolution. The full-disk image, which uses the three coarsest subcollimators, shows the characteristic ringed patterns caused by incomplete sampling of the Fourier plane. Noteworthy is the "mirror" source seen in the lower left quadrant of the full-disk map. This is an effect of not having both "sine" and "cosine" subcollimators, but is readily corrected for in the maps. The true source in this case is on the limb in the upper right. Exactly halfway between the true and mirror sources is the spin axis, where no modulation occurs. The small-field back-projection map, made with subcollimators 3-8, shows the flare surrounded by rings, whose amplitude is smaller than in the full-disk map due to the use of a larger number of subcollimators.

All of the practical image reconstruction algorithms for improving a back-projection ("dirty") map are nonlinear, since linear deconvolution algorithms such as Wiener filtering and inverse filtering are inapplicable to applications such as *RHESSI* which do not completely sample

the Fourier plane. In the following section, we describe some of the nonlinear options currently implemented.

4.2. CLEAN

CLEAN is an iterative algorithm which deconvolves a Point Spread Function—the imager's response to a delta function source—from a "dirty map". This algorithm is of fundamental importance in radio astronomy, where it is used to create images of astronomical sources obtained with interferometers. The basic CLEAN method was developed by Högbom (1974). It was originally designed for point sources, but it has been found to work well for extended sources as well when given a reasonable starting model. The Högbom CLEAN constructs discrete approximations to the CLEAN map in the plane from the convolution equation,

$$\mathcal{P} \otimes I_{source} = D \tag{7}$$

where $\mathcal{P}$ is the *RHESSI* PSF for one or many subcollimators and/or harmonics, I_{source} is the source distribution, D is the dirty map, and $\otimes$ denotes a convolution.

The algorithm goes as follows:

Start with an initial approximation I_0; copy it to a new image, called the residual map. Search for the largest value in the residual map, saving the position in a "CLEAN component" table. Center a delta function at the location of the largest residual flux and give it an amplitude μ (the so-called "loop gain") times this value. Subtract the scaled Point Spread Function $\mathcal{P}$ from I_{n-1} to yield I_n. Continue this iteratively until a specified iteration limit is reached, or until the peak residual or RMS residual decreases to some level.

In the resulting final map (I_{final}), it is assumed that the residual brightness distribution consists mainly of noise. To damp out high spatial frequency features which may be spuriously created in the iteration, one convolves each CLEAN component with the so-called CLEAN PSF, $\mathcal{P}_{clean}$ (the "CLEAN beam" in radioastronomy), which is simply a suitably smoothed version or inner portion of the PSF, $\mathcal{P}$.

$$I_{clean} = I_{final} \otimes \mathcal{P}_{clean} \; + \; \{D - \mathcal{P} \otimes I_{final}\} \tag{8}$$

A CLEAN map is produced when the final residual map is added to the approximate solution, in order to include the noise.

The main disadvantage of CLEAN is that it does not (at least in the Högbom version) compare the observed modulation profile with

a model modulation profile to assess the "goodness of fit" during the iteration. Two variants of CLEAN exist for *RHESSI*. One is for rectangular coordinates, and the other is for polar coordinates. In most circumstances, the latter has a significant advantage of speed over the former.

Figure 6 shows examples of back projection, CLEAN, MEM-Sato, MEM-vis, PIXON, and Pixelized-Forward-Fit maps, all derived from a simulated event list derived from a double source.

4.3. Maximum Entropy Methods

The principle of Maximum Entropy is to find the map which is maximally noncommittal with regard to the unavailable information, i.e. the regions of the Fourier plane for which *RHESSI* has no data. The image to be found is the smoothest one that fits the data to within the noise level.

HESSI's observations are provided in the form of nine sets of counts in time bins, each time bin corresponding to a particular roll angle. The aim is to find an image that is consistent with these counts to within the photon counting noise. Since there can be many images consistent with the observations, MEM is designed to find the smoothest such image. Traditionally, consistency is measured using a χ^2 measure on the counts:

$$\chi^2 = \sum_i \frac{(\mathcal{C}_i - \mathcal{E}_i)^2}{\sigma_i^2} \tag{9}$$

where $\mathcal{C}_i$ is the count for time bin i and $\mathcal{E}_i$ is the "expected" count from the reconstructed image, and σ_i is the estimated error of count $\mathcal{C}_i$. If only photon counting noise is important then $\sigma_i^2 = \mathcal{E}_i$, but in practice systematic errors and uncertainties in the background may also be important and so should be included in σ_i.

The smoothness of the image is quantified using an entropy measure. In one view, the entropy is a quantity which, when maximized, produces a positive image with a compressed range in pixel values (Cornwell 1984), but according to Gull and Skilling (1984) and Sivia (1996) the only function which guarantees that no unwanted correlation is imposed is:

$$\mathcal{H} = -\sum_m F_m \log F_m \tag{10}$$

where F_m is the flux in pixel m. A smooth image will have a larger $\mathcal{H}$. The goal of MEM is to find the smoothest image that fits the data.

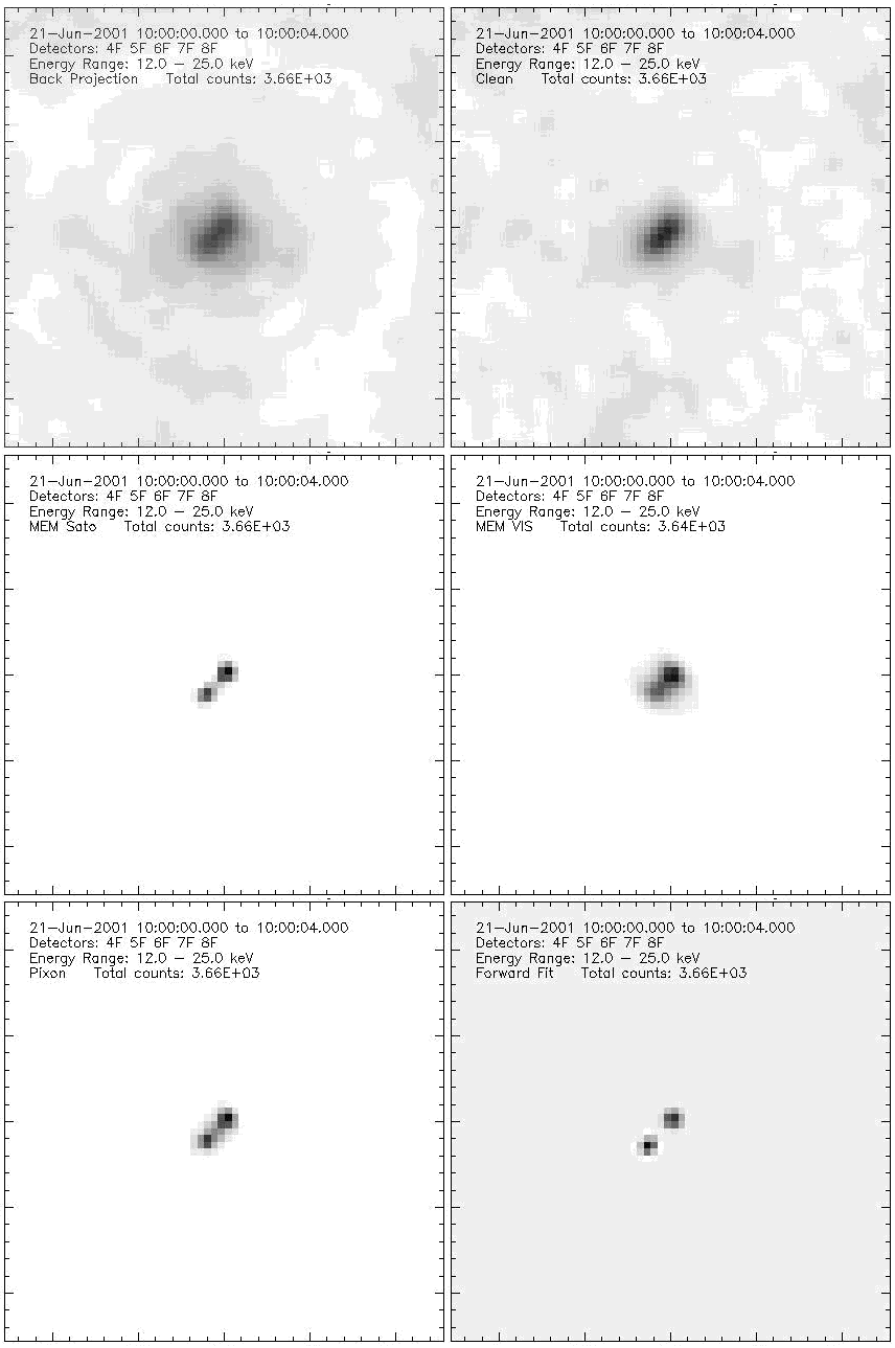

Figure 6. Example Back-projection, CLEAN, MEM-Sato, MEM-vis, PIXON, and Pixelized-Forward-Fit maps.

In practice, this means maximizing $\mathcal{Q} = \mathcal{H} - \frac{\lambda}{2}\chi^2$ for the smallest possible λ. The idea is that λ is set to a small value to begin with and an image is sought iteratively that has $\chi^2 = 1$, i.e. it is consistent with observations. If such an image cannot be found, the smoothness constraint is probably too strong, and so λ is increased to allow a less smooth image. Additional constraints (*e.g.* total flux) can be added to $\mathcal{Q}$ if desired.

MEM has had a rich history as the main imaging algorithm used for image reconstruction with Yohkoh's HXT. Although the details of implementation are somewhat different for *RHESSI,* the basic theory is still relevant (Sato, 1998, Sato, Kosugi, and Makishima, 1999).

Another *RHESSI* image reconstruction algorithm, MEMVIS, applies MEM to the visibilities rather than the counts. The advantages of using visibilities are discussed in the Appendix. Before iterations begin in MEMVIS, the counts are converted to visibilities, correcting for the wandering of the spin axis. With this correction applied, the modulation patterns, and therefore the processing per iteration, are greatly simplified. The basic MEM equations outlined above need some alteration because visibilities are complex quantities. For example, the real and imaginary parts in the χ^2 sum must be separated, and the constraints must be reformed to avoid $\mathcal{Q}$ being complex. The MEM algorithm then proceeds according to the steps described above.

The main advantages of MEMVIS is its efficiency (lower memory requirements, use of fast Fourier transforms) and the ease in which the visibilities that it uses can be integrated over time (by *literally* just adding them together). It is apparent from many simulations that MEMVIS appears to be remarkably robust at low count rates.

Figure 7 shows example MEMVIS and MEM-SATO maps.

4.4. Forward-Fitting

The forward-fitting method is based on models that represent a spatial map by a superposition of multiple source structures, which are quantified by circular Gaussians (4 parameters per source), elliptical Gaussians (6 parameters per source), or curved ellipticals (7 parameters), designed to characterize real solar flare hard X-ray maps with a minimum number of geometric elements. Examples of fits to hard X-ray sources may be seen in Aschwanden *et al.*, 1999.

In one realization of this scheme, maps of superimposed Gaussians are created iteratively, at each step constructing a model modulation profile from the map. In this "pixelized" form, the map evolves into a best fitting image.

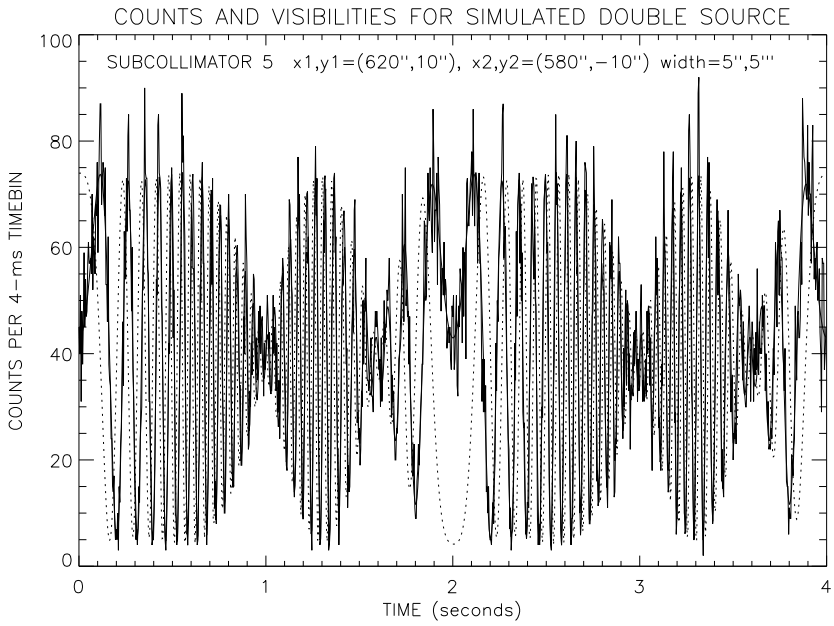

Figure 7. Fits to visibilities deriving from simulated count rate profiles for a double source of 10,000 counts/s/SC. The solid curve is the real part of the visibility, and the dotted curve is the imaginary part. Note the beating of the sources, which are about 1.5 angular pitches apart.

In another realization of forward-fitting, there are no maps computed at intermediate steps. The algorithm uses the beat patterns seen in the modulation patterns to infer the characteristics of the source. The most efficient way to do this is to compute the visibilities from the count profiles (after selecting map center and calibrating). Then a phase-shift to map center eliminates the rapid modulations, leaving only the low-frequency beat patterns. For two circular Gaussians, the extrema of the beat patterns then provide the relative separation and strengths of the sources. The ratios of the beat strengths for successive subcollimators determine the Gaussian widths. The inferred parameters of the source then provide model modulation profiles for comparison with the observed profiles. Chi-square determinations assess the goodness of fit for iterative estimations of the strength of further sources. Figure 7 shows fits to visibilities deriving from simulated count rate profiles for a double source of 10,000 counts/s/SC. In principle, fits such as this can yield the flux, positions and widths of two Gaussian sources, and possibly more if the fluxes are sufficiently high.

4.5. The PIXON Method

The PIXON method is another technique which removes the sidelobe pattern of a telescope while mitigating the problems of correlated residuals and spurious sources which are commonly seen in Fourier deconvolution, chi-square fitting, and maximum entropy approaches.

The goal of the Pixon method is to construct the simplest, i.e. smoothest, model for the image that would be consistent with the data, i.e. have an acceptable chi-square fit. Being the simplest model, the derived image would be artifact free, i.e. there would be no spurious sources. In addition, it is claimed by PIXON proponents that the model is necessarily most tightly constrained by the data, and consequently has the most accurately determined parameters.

The PIXON method changes the global smoothness idea of MEM into a local condition in which local maximum smoothness of the image is imposed. From an information science point of view, one selects a model with the minimum information content from the family of multiresolution basis functions (pixons) and which statistically fit the data.

Since the model has minimum complexity, spurious sources are unlikely to arise. Each parameter is determined using a larger fraction of the data, hence it is, presumably, determined more accurately. It is claimed that this usually results in superior photometric and positional accuracy, and that, since the minimum number of parameters are used, the data cannot be over fitted. PIXONS, however, pays a price for its photometry: the method is about two orders of magnitude slower than the other reconstruction methods. Therefore, as with Yohkoh/HXT, it will probably be used only after the faster reconstructions have produced maps, and when checking the strength or shape of weak sources is required.

5. Imaging Performance

5.1. Imaging Strengths and Limitations

Although it is too early in the mission to provide a definitive summary on the imaging performance, the general properties of *RHESSI* imaging can be broadly outlined. This is particularly important since RMC imaging has very distinctive strengths and weaknesses compared to conventional imaging instruments and these properties are directly relevant to the kind of science that can be done with RMC imaging.

RHESSI imaging was not designed to provide images with the kind of morphological richness and detail that we have come to expect from Yohkoh/SXT, TRACE, SOHO/EIT and other direct imaging instruments. Instead, *RHESSI* imaging determines the flux, location, size and shape of the dominant source components. Its measure of image quality is 'dynamic range', defined as the ratio of the surface brightness of the strongest source to the weakest credible source in the field of view. The design goal (and current expectation) is that in favorable circumstances dynamic range of 100:1 can be achieved.

In general, *RHESSI* imaging has proved to be remarkably robust, a feature which permitted the generation of viable images early in the mission.

There are four broad factors that limit the quality of *RHESSI* imaging. The first is the specific spatial frequencies that are measured. The limitation of nine spatial frequencies provides a fundamental limit to the complexity of the images that can be generated. This limitation becomes more severe if imaging is done on timescales of less than one half of the rotation period.

Photon statistics are an important constraint. In favorable circumstances, a point source can be detected and located with as few as 300 counts. However, usually $\sim 10^3$ are required and for more pleasing images it is preferable to have $\sim 10^4$ or $\sim 10^5$ counts.

As we have seen, the imaging algorithms ultimately rely upon comparisons of observed count rates to 'predictions' based on convolving test maps with instrument response. Therefore, in circumstances with good statistics and simple sources, the knowledge of the grid and detector response can provide the limitation. The grid response, to be described in detail in a future paper, is believed to be known at the $\sim$2 percent level. Good progess continues to be made in understanding the detector response (Smith *et al.*, 2002), which is very relevant at high count rates. For example, it has long been known that pileup (where the superposed signal of two simultaneous low-energy photons is detected as a single higher-energy photon) can introduce artifacts in the perceived photon spectrum. Since rate of low-energy photons is modulated, a consequence for imaging is that the pileup of low-energy photons can superimpose a low-energy image onto an image made at higher energies. This has been observed in cases where the count rates are particularly high.

The fourth factor is assumptions that are implicit in the imaging algorithms. Such assumptions include: the short duration of time bins compared to the modulation period; the uniformity of instrument re-

sponse over the selected energy range; and the uniformity of instrument response over the imaging field of view.

The strengths of this imaging technique include the ability to accurately (∼1 arcsecond) locate the source components on the Sun. This supports both accurate co-location with images in other wavelengths, and reliable comparisons of images as a function of time and energy. (Note that *RHESSI's* imaging from 3 to 15000 kev uses a common set of 'optics'.)

Photometric reliability of *RHESSI* images depends on the circumstances, but is often at the $\sim$ 10 percent level. This is sufficient to support some feature-based imaging spectroscopy.

Source sizes can also be determined, although at present this requires careful interpretation with some algorithms.

Finally, one of the underlying strengths of *RHESSI* imaging, discussed by Schwartz *et al.* (2002) and derived from the photon-based nature of the data, is the ability to select the time resolution, energy resolution, imaging field of view, resolution and reconstruction technique. These choices can be optimized at the time of analysis, in a manner that depends on the characteristics of the flare and on the specific science objectives. In practice this is perhaps one of the most valuable and novel features of *RHESSI* imaging.

5.2. Self Calibration

As discussed above, one of the potential limitations of *RHESSI* imaging is the knowledge of the grid response. However, one of the features of *RHESSI* imaging is that there are several ways to self-calibrate amplitudes and phases. While this feature will be discussed more fully in a future paper, it is perhaps worth mentioning the progress made to date. In particular, the relative 'phases' of the grids is a vital parameter. For each grid this represents the average position of the center of the slats with respect to the imaging coordinate system defined by the solar aspect system. The current determination of these phases is based on maximizing the response of the system to unresolved sources. The accuracy of these determinations appears to be $\sim 10^2$ of the grid pitch. A more sensitive technique, based on the stability of imaging with even and odd half rotations, will be used to improve this further.

Other grid response parameters, such as the average transmission, can be verified by comparison of spatially integrated spectra obtained from the 9 detectors. Interpretation of these ratios as a function of energy and offset angle can be used to fine tune the grid parameters.

5.3. Expected Evolution of Imaging

During the course of the *RHESSI* mission, lessons are being learned about unanticipated features of the hardware and software. Examples of such lessons to date are the data gaps (Smith *et al.*, 2002). As in other missions, the imaging software is expected to improve as bugs are eradicated and better algorithms are developed. In particular, we anticipate introducing an alternate approach to summing time bins which will greatly facilitate integration over long time periods. Also, the neglected 2nd and 3rd harmonics of the grid response will be taken into account. For strong flares, this has the potential to improve the angular resolution of the grids by factors of 2 and 3 under favorable circumstances.

An important feature of these improvements is that in all cases, they will be applicable retroactively to data acquired from the start of the mission.

6. Appendix: Visibilities

The concept of visibilities is borrowed from radio astronomy. In the context of *RHESSI*, 'counts' and 'visibilities' can be regarded as two time series that present the same information: the response of *RHESSI to* a brightness distribution. The 'visibilities', however, come in pairs: one is a 'count' profile much like the real *RHESSI* count profile (but with imperfections calibrated out), and the other is also a 'count' profile from an ideal subcollimator shifted 90° in phase from the real one.

In radio astronomy the response of an interferometer to point sources in the sky, known as the fringe pattern, can be quantified in terms of complex visibilities, which are the components of a discrete Fourier (*i.e.* cosine and sine) transform of the sky. Thus far we have considered the response of *RHESSI* to a point source as a modulation profile (e.g. Figure 3, top panel), expressed as a time series of counts. The modulation profile can be obtained from the brightness distribution using the modulation patterns, which we have represented in terms of a cosine and a series of harmonics. Clearly *RHESSI* imaging has much in common with radio astronomy interferometry and could benefit from the enormous efforts invested in that subject. Also, we will see that the use of visibilities with *RHESSI* has several intrinsic advantages. To exploit this resource it is necessary to consider what a visibility means in relation to counts in the context of RHESSI.

6.1. THE (U,V) PLANE

In radio astronomy the visibility of a point source of flux F_0 at coordinate (x_0, y_0) is defined to be the Fourier transform:

$$\mathcal{V}(u,v) = F_0 \; cos(2\pi\{ux_0 + vy_0\}) + i \; F_0 \; sin(2\pi\{ux_0 + vy_0\}) \qquad (11)$$

The cosine term on the right side of this equation is the count rate from an idealized *RHESSI* subcollimator (with the mean subtracted out) and the sine term is a hypothetical count rate (again with the mean subtracted out) for another ideal subcollimator with pointing shifted half an angular pitch (90° in phase) with respect to the first subcollimator.

The variables (u, v) are the coordinates in the Fourier plane and the 2D array $\mathcal{V}(u, v)$ is the Fourier transform of the flux distribution in the x-y source plane, in this case containing a single point source at (x_0, y_0). It turns out that detector k, while *RHESSI* is at roll angle α_i, will sample a quantity closely related to the visibility transform $\mathcal{V}_{ik} = \mathcal{V}(u_{ik}, v_{ik})$ at $u_{ik} = cos\alpha_i/p_k$ and $v_{ik} = sin\alpha_i/p_k$.

So, each observation (count integrated over a time bin) that *RHESSI* makes is a sample upon one of nine possible circles, one circle for each detector. Samples on the largest circles correspond to the highest spatial frequencies, and come from detectors with the small pitches. In one rotation, for a particular detector, *RHESSI's* observations form a time series of count values, where each time corresponds to a particular roll angle. This time series is a set of sample points spread across the entire circumference of one of the nine circles. In this way the count time series can be related to the 2D Fourier transform of the source flux distribution. Conversely, the visibilities, which are the samples of the 2D Fourier transform, can be regarded as a time series in the context of *RHESSI*.

If the spin axis is fixed so that (a_n, Ψ_n) are constant, if background is negligible, and if the transmission T and livetimes τ are constant, then the relation between the fundamental term in the counts and visibilities can be deduced from Equations (4), (5) and (6):

$$\mathcal{X}_{ik} \;\equiv\; Real\,[\mathcal{V}_{ik}] = \frac{\mathcal{C}_{ik} - F_0 T\tau}{T\tau a_1} = F_0 \cos\Phi_{ik} \qquad (12)$$

In this idealized case, the counts are the cosine transform of the image. The imaginary part of the visibility is the corresponding sine transform. Figure 7 shows the real part of the visibility time series, i.e. the *visibility modulation profile*, for a point source. The dashed lines in

that figure show the imaginary part of the visibility (offset by the mean flux, since their mean must be zero). The case of a moving spin axis, important for constructing visibilities from observed counts in practice, is dealt with in Section 6.2.

The importance of visibilities to *RHESSI* is that they are an intermediate between the observed counts and images. The visibilities have been corrected for all of the spin-axis wobble, slit-shadowing, transmission and deadtime effects. Consequently, visibilities, unlike count-rate profiles, can be added from one rotation to another.

¿From many simulations, the advantages and some disadvantages can be summarized as follows: (1) The aspect correction can easily be applied while constructing visibilities from the observed counts. (2) Due to 1, visibility modulation patterns do not need to be corrected for the aspect solution for each time bin. (3) Due to 2, operations involving modulation patterns can be performed with a convolution based on Fast Fourier Transform methods, rather than a matrix multiplication. This allows a speed-up of order M^2 as compared to $M \log M$, where M is the number of time bins. (4) Due to 2, integration of visibility values over several rotations simply involves adding together visibility series from those rotations. (5) In constructing visibilities from observed counts, there is effectively a smoothing, which relaxes problems arising from the presence of zero counts. The price is the introduction of a small systematic error and a correlation of noise on visibilities in neighboring time bins.

6.2. From Count Rates to Visibilities

We now discuss the method by which the visibilities can be constructed from the counts. For simplicity, we discuss only the fundamental term in the Fourier expansion of the count rate. Constructing the visibilities needs to be done in the context of making a map, i.e. reconstructing an image, in a limited spatial region of interest, e.g. a solar flare on the Sun's disk. Central to this is the concept of the *phase at map center* Φ_0, touched on in Section 4.s. In general, Φ_0 depends on the results of the aspect solution, the time binning, the subcollimator, and the position of the map center. The phase at map center (x_0, y_0) can be calculated from Equation (5):

$$\Phi_0 = \Phi(x_0, y_0) - \Phi(x_s, y_s). \tag{13}$$

$\Phi(x_s, y_s)$ is the phase correction arising from the fact that the map center (x_0, y_0) and the projected position of the subcollimator on the source plane (x_s, y_s) are at different locations. Using the aspect system

data, the distance of the line of maximum transmission from map center is computed for each roll angle α_i and each subcollimator pitch p_k. This gives the phase at map center for each time bin i, detector k. (See Figure 4.)

Given an incident flux of photons on a *RHESSI* subcollimator, after the selection of a map center, the predicted count rate $\mathcal{C}$ of a point source located at map center is given by Equation (6), i.e., dropping the subscripts j, k for clarity:

$$\mathcal{C}_i = F_0 T_i \tau_i \cdot \left(1 \; + \; a_1^i \; cos[\Phi_0^i]\right) \tag{14}$$

The visibility of a point source at the map center is:

$$\mathcal{V}_i = F_0 e^{i\Phi(x_0,y_0)} = F_0 e^{i(\Phi_0^i + \Psi_1^i)} \tag{15}$$

Note that the visibility *does not* depend on the subcollimator coordinates (x_s, y_s), but the count rate *is* subject to phase shifts caused by telescope motion. Comparing Equations (15) and (16) leads to the following relation between counts and visibilities:

$$\mathcal{X}_i \;\equiv\; Re\left[\mathcal{V}_i e^{-i\Psi_1^i}\right] = \frac{\mathcal{C}_i - F_0 T_i \tau_i}{T_i \tau_i a_1^i} \tag{16}$$

where T_i, τ_i and a_1^i are known quantities, but F_0 is unknown. There are various ways to estimate F_0 and the optimum method in the presence of background has not yet been decided on.

Once F_0 has been determined, the conversion from counts to visibilities depends on oversampling of the circles in the UV plane. In each modulation cycle, there must be at least four time bins. During each cycle, the rotation of the modulation pattern within the map can be thought of as a purely linear shift. So for each successive 4 (or more) count rates, one may represent the position in the (u, v) plane by its average value $(\bar{u_i}, \bar{v_i})$ and an offset δ. Then the corrected count rate (Equation 17) can be represented as the cosine transform:

$$\mathcal{X}_i = \int\int cos(2\pi[\bar{u_i}(x - x_0) + \bar{v_i}(y - y_0)] + \delta_i) f(x, y) dx dy \tag{17}$$

The angle δ_i changes by 360° during one cycle, so we can easily have 4 or more independent samples; a regression fit to each modulation cycle then gives both the sine and the cosine components $\mathcal{X}_i^{sin}$ and $\mathcal{X}_i^{cos}$.

It is worth mentioning that in early versions of RMC design, there were both sine and cosine subcollimators (*e.g.*, Mertz *et al.* 1986, Murphy, 1990), but, as we see here, this turns out not to be necessary in

hardware, since with sufficient sampling of the modulation profile, relative amplitudes of the sine and cosine components can be determined from the modulation profile itself.

It is important to note that, according to Equation (17), the peak-to-peak variation of the visibility is several times larger than the peak-to-peak variation of $\mathcal{C}$. This is because the visibility reflects the transform of the flux distribution at the front grid, while the count rate is the modulated profile of the photons reaching the detector. In fact, when the livetime is unity ($\tau_i = 1$), and when the subcollimator pattern is perfectly triangular, ($a_1^i T_i = 2/\pi^2$), the peak-to-peak variation of $Re[\mathcal{V}_i]$ is $\pi^2/2 = 4.9$ times that of the count profile.

For a more general case, where the source is an arbitrary superposition of N point sources of flux F_j at locations (x_j, y_j), the visibility is found by summing Equation (16) over the sources. The generalization to higher harmonics is simple, and is important for achieving the highest possible resolution and for self calibration, but the details are beyond the scope of this paper.

7. Acknowledgements

We wish to take this opportunity to thank the PSI team led by Alex Zehnder, and Dave Clark and his colleagues at GSFC for the care and technical expertise they used in fabricating the imager. This work is supported by NASA grant NAS5-98033-05/03.

References

Aschwanden, M., *et al.*., 2002: *Solar Phys.*, this volume.

Aschwanden, M., Fletcher, Sakao, Kosugi, and Hudson, 1999: *Astrophys. J.* 517, 977, 1999.

Bester and Lewis, 2002: *Solar Phys.*, this volume.

Cornwell, T. J., in *Indirect Imaging, Proc. IAU/URSI Symp.*, ed. J.A. Roberts, Cambridge Univ. Press, 291, 1984.

Crannell , C. J., Hurford, G. J., Orwig, L. E., and Prince, T. A., 1986: SPIE 571, 142. Crannell,C.J., American Institute of Aeronautics and Astronautics: Washington DC, AIAA-94-0299, 1994.

Curtis, D., *et al.*., 2002: *Solar Phys.*, this volume.

Durouchoux, P., Hudson, H., Hurford, G., Hurley, K., Matteson, J., and Orsal, E., 1983: *Astron. Astrophys.* 120, 150.

Enome, S., 1982: *Adv. Space Res.* 2/11, 201.

Gull, S. F. and Skilling, J., 1984: 131, 646.

Högbom, J. A., 1974: *Astron. Astrophys.* 15, 417.

Holman, G. D. *et al.*, 1997: *Bull. AAS*, 191, 7416.

Hurford, G. and Curtis, D., 2002: *Solar Phys.*, this volume.
Kilner, J.R. and Nakano, G.H., 1991: S.P.I.E. 1159, "EUV, X-Ray, and Gamma-Ray Instrumentation for Astronomy and Atomic Physics", 27.
Kosugi, T., Masuda, S., Makishima, K., Inda, M., Murakami, T., Dotani, T., Ogawara, Y., Sakao, T., Kai, K., Nakajima, H., 1991: *Solar Phys.* 136, 17.
Lin, R., and Dennis, B., 2002: *Solar Phys.*, this volume.
Lin, R. P., Dennis, B. R., Emslie, A. G., Ramaty, R., Canfield, R., and Doschek, G., 1993: *Adv.Space Res.* 13/9,401.
Lin, R. P., Dennis, B. R., Ramaty, R., Emslie, A. G., Canfield, R., and Doschek, G., 1994: Geophysical Monograph 84, Washington DC:AGU, 283.
Lin, R. P., *et al.*, 1998: SPIE 3442, p.2.
Makishima, K., Miyamoto, S., Murakami, T., Nishimura, J., Oda, M., Ogawara, Y., and Tawara, Y., 1977: in *New Instrumentation for Space Astronomy*, (K.A. van der Hucht and G.Vaiana eds.), New York: Pergamon Press.
Mertz, L. N., 1996: "Excursions in Astronomical Optics", Springer-Verlag New York.
Mertz, L. N., 1967: Proc. Symp. on Modern Optics, v. 17 of the *Microwave Research Institute Symposia Series* (Polytechnic Institute of Brooklyn), New York.
Mertz, L. N., Nakano, G. H., and Kilner, J. R., 1986: *J. Opt. Soc. Am.* 3, 2167.
Murphy, M. J., 1990: *Nucl. Instr. and Methods in Physics Research*, A290, 551-558.
Ohki, K., Tsuneta, S., Takakura, T., Nitta, N., Makishima, K., Murakami, T., Ogawara, Y., Oda, M., Miyamoto, S., 1982: Proc. Hinotori Symp. on Solar Flares, ISAS, Tokyo, Japan, p. 102.
Palmer, D. and Prince, T. A., 1987: *IEEE Trans. Nucl. Sci.*, NS-34, No. 1, 71.
Prince, T. A., Hurford, G. J., Hudson, H. S., and Crannell, C. J., 1988: *Solar Phys.* 118, 269.
Sato, Jun, 1988: PhD Thesis, NAO.
Sato, J., Kosugi, T., Makishima, K., 1999: PASJ, 51, 127.
Schmahl, E. J., AGU meeting, May, 1998.
Schwartz, R. *et al.*, 2002: *Solar Phys.*, this volume.
Sivia, D.S., 1996: *Data Analysis, a Bayesian Tutorial*, Clarendon Press, Oxford.
Schnopper, H. W., Thompson, R. I., and Watt, S., 1968: *Space Sci. Rev.* 8, 534.
Schnopper, H. W., Bradt, H. V., Rappaport, S., Boughan, E., Burnett, B., Doxsey, R., Mayer, W., Watt, S., 1970: *Astrophys. J.* 161L, 161.
Smith, D. *et al.*., 2002, *Solar Phys.*, this volume.
Van Beek, H. F., Hoyng, P., Lafleur, B., and Simnett, G. M., 1980: *Solar Phys.* 65, 39.
Zehnder, A., Fivian, M. and Henneck, 2002: *Solar Phys.*, this volume.